Received December 12, 2015, accepted December 30, 2015, date of publication January 12, 2016,
date of current version January 22, 2016.

Digital Object Identifier 10.1109/ACCESS.2016.2517400

Experimental Multipath-Cluster Characteristics of 28-GHz Propagation Channel

XUEFENG YIN[1], CEN LING[1], AND MYUNG-DON KIM[2]
[1]College of Electronics and Information Engineering, Tongji University, Shanghai 201804, China
[2]Electronics and Telecommunications Research Institute, Daejeon 34129, Korea

Corresponding author: X. Yin (yinxuefeng@tongji.edu.cn)

This work was supported in part by the National Natural Science Foundation of China under Grant 61471268, in part by the Information and Communication Technologies (ICT) Research and Development Program within the Ministry of Science, ICT and Future Planning/Institute for Information and Communications Technology Promotion, through the Project entiltled Development of Core Technologies to Improve Spectral Efficiency for Mobile Big-Bang, Korea, and in part by the Hongkong, Macao, and Taiwan Science and Technology Cooperation Program of China under Grant 2014DFT10290.

ABSTRACT In this paper, a channel measurement campaign is introduced, which utilizes direction-scan-sounding to capture the spatial characteristics of 28-GHz wave propagation channels with 500-MHz sounding bandwidth in office environments. Both line-of-sight and non-line-of-sight scenarios were considered. Measurements were performed by fixing a transmit pyramidal horn antenna, and rotating another one in the receiver site at 10° steps in azimuth. The antenna outputs are viewed as array signals, and a space-alternating generalized expectation-maximization (SAGE) algorithm is applied to estimate delay and angular parameters of multipath components. Benefiting from high resolution achieved by using the SAGE and deembedding of antenna radiation pattern and system responses, more multipath clusters with less spreads in delay and azimuth are found per channel compared with existing works on 28-GHz propagation. The statistics of channel parameters extracted here constitute a preliminary stochastic multipath-cluster spatial channel model.

INDEX TERMS Direction-scan-sounding, millimeter wave propagation, channel measurement, horn antenna, SAGE, and multipath cluster.

I. INTRODUCTION

The increasing demand in high-data-rate communications for the fifth generation (5G) wireless systems prompts the necessity of signal transmission on higher frequency band (HFB) beyond 6-GHz, because of abundant spectrum resources potentially available in HFBs [1]. For example, the 7th European framework project ''Mobile and wireless communications Enablers for the Twenty-twenty Information Society (METIS)'' has proposed for 5G communications a candidate frequency band ranging from 450 MHz to 85 GHz [2]. Conventional channel characterization for HFB focuses on 60 GHz millimeter (mm-) wave indoor propagation [3]–[10]. Large-scale characteristics, e.g. path-loss, shadow fading, frequency selectivity, and influence of human body have been investigated [7]–[10]. High-resolution parameter estimation (HRPE) algorithms, such as Space-Alternating Generalized Expectation-maximization (SAGE) [11] and Richter's MAXimum likelihood estimation (RiMAX) [12] were adopted to extract multipath components (MPCs) from the outputs of virtual linear or planar arrays in 60 GHz channel measurements [13]–[15]. Multipath clusters were identified and their statistics have been presented as stochastic channel models for certain propagation scenarios [15], [16].

Recently, multiple channel measurement campaigns for more frequencies in HFB have been carried out, such as 10–11 GHz [6], [17], [18], 28-38 GHz [19]–[25], 70-73 GHz [26]–[29], and 81-86 GHz [28]. In these campaigns, antennas with narrow Half-Power-Beam-Width (HPBW), e.g. pyramidal horn antennas, were used [27], [29], [30]. One motivation of adopting narrow-HPBW antennas in measurements is that the large antenna gain can compensate the significant path-loss in HFB propagation. Furthermore, a direction-scan-sounding (DSS) method can be used by rotating the antenna towards different directions in such a way that a spatial channel is ''scanned'' in multiple directions. Power delay profiles (PDPs) and path-loss models for omni-directional channels have been

IEEE Access
The journal for rapid open access publishing

synthesized from those directional observations, based on which channel models were proposed for outdoor cellular, back-haul, and indoor propagations scenarios [31]–[33]. However, without de-embedding of antenna radiation pattern, the models obtained in these works are subject to the DSS settings, such as the number of scanning steps and the size of scanning step [27], [30], [34]. Only recently, HRPE using the SAGE algorithm was applied to estimating azimuths of arrival (AoAs) and delays of MPCs from DSS measurement data for 28 GHz channels [21]. However, as the antenna radiation pattern adopted was obtained via simulation rather than being measured in anechoic chamber, a large amount of spurious MPCs are obtained. Consequently, the models established do not represent the exact properties of propagation channels.

In this paper, a channel measurement campaign recently conducted in an office of Eletronics and Telecommunications Research Institute (ETRI), Daejeon, Korea, is introduced, which makes use of DSS for channel sounding at center frequency of 28 GHz and bandwidth of 500 MHz. Different from previous channel investigation based on non-parametric approaches [6], [19], [26], [28], a SAGE algorithm is implemented to estimate MPCs' parameters from channel impulse responses (CIRs) at the output of sliding-correlator [35]. The statistics of composite channel and cluster-level parameters are extracted and compared with existing works and standard channel models for lower frequency bands. From these results, a cluster-based stochastic spatial channel model (SCM) is established with antenna- and system-responses de-embedded. It is worth mentioning that the work presented here is only a part of a series of channel characterization activities conducted by ETRI. Those activities include outdoor measurements in dense urban districts in Gangnam, Seoul and in Daejeon, indoor measurements in Seoul railway station and Incheon airport at both 28 and 38 GHz. Instead of presenting a statistically sound model based on a sufficient amount of measurements, our studies presented here focus more on the applicability of HRPE-based parameter estimation and the cluster-based characterization in mm-wave channel modeling. They can be implemented to construct channel models for various environments and from different perspectives, e.g. cross-polarized channel characteristics, channel consistency, etc..

The rest of the paper is organized as follows. In Section II, the measurement campaigns and equipment are introduced. In Section III, the derived SAGE algorithm is described, and the examples of estimated MPCs are presented. Section IV elaborates the MPCs' constellation and the characteristics of composite channels for different propagation scenarios. Section V introduces a clustering method and the statistics of cluster characteristics extracted. Finally, conclusive remarks are given in Section VI.

II. MEASUREMENT ENVIRONMENT AND SETUP

Fig. 1 illustrates a DSS approach adopted in our measurement which is similar with those applied in [20], [33], and [36].

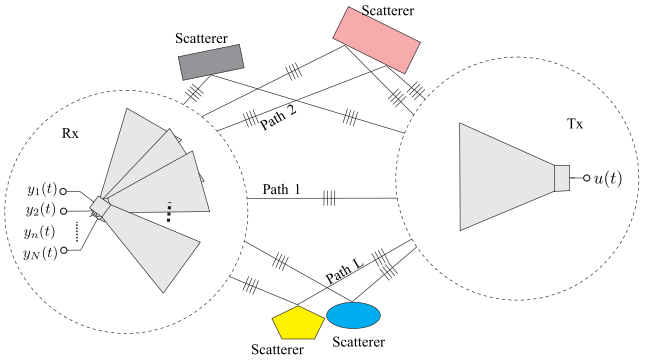

Fig. 1. A diagram of direction-scan channel sounding by using horn antennas, where $u(t)$ is the sounding signal, and $y_n(t)$, $n = 1, \ldots, N$, is the received signal obtained with Rx antenna directed to N orientations.

The Tx and Rx are equipped with 60°- and 10°-HPBW pyramidal horn antennas respectively. During measurements, the Tx antenna is fixed, and the axis of the Rx horn antenna is rotated in the step of 10° in azimuth from 0° to 360° and in co-elevation from −10° to 10°.[1] Thus, for each measurement cycle, $36 \times 3 = 108$ CIRs are obtained, which can be viewed as the outputs of a virtual antenna array with antenna elements oriented towards multiple directions.

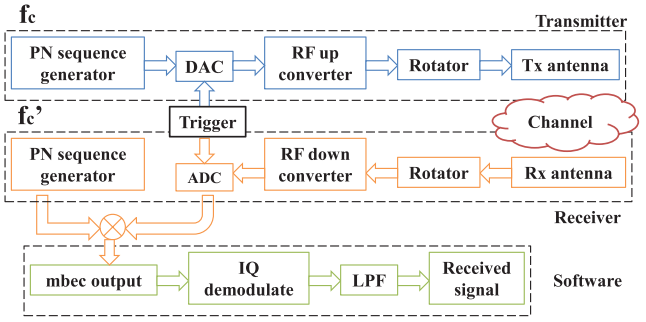

Fig. 2. Block diagram of the underlying measurement system.

The block diagram of the channel sounder - millimeter-wave Band Exploration and Channel sounder (mBEC)- used in the measurements is illustrated in Fig. 2. The Tx transmits periodically a pseudo-random (PN) m-sequence generated by a 12-order shift register in the transmission rate of 500 Mega chip-per-second (Mcps). This results in an intrinsic delay resolution of 2 nanoseconds. The PN sequence is modulated with Binary Phase Shift Keying (BPSK) and up-converted to the carrier frequency of 28 GHz. The rotation of the Rx antenna is controlled by a software which also records the antenna attitude in real-time. In the Rx site, the signal is down-converted and fed into an analog-digital convertor (ADC).

[1] In [21] and [33], the so-called best channel which has the strongest received signal strength is first detected by rotating both Tx and Rx antennas. Then the axes of these antennas are considered to be the directions of 0°-azimuth and 0°-coelevation. This is considered unnecessary in our case, as we intend to observe the channel characteristics in a fixed coordinate system irrespective of the antenna orientation.

The output is correlated with the same PN sequence with chip rate of 499.96 Mcps, and then low-pass-filtered to generate CIRs as described in [30], [37] and [38]. During the sounding procedure, the Tx and Rx are fully synchronized through a common triggering module. Table 1 reports some specifications used in the measurements.

TABLE 1. Measurement configuration.

Receiver		Transmitter	
Antenna HPBW	10°	Antenna HPBW	60°
Frequency (GHz)	27.75-28.25	Frequency (GHz)	27.75-28.25
Antenna gain	24.4 dBi	Antenna gain	9.9 dBi
Step in azimuth	0° : 10° : 350°	Fixed azimuth	
Step in elevation	−10°, 0°, 10°	Fixed at 0° co-elevation	
Dynamic range of received CIRs	54 dB	Num. of chips	4095
		Transmit power	27 dBm

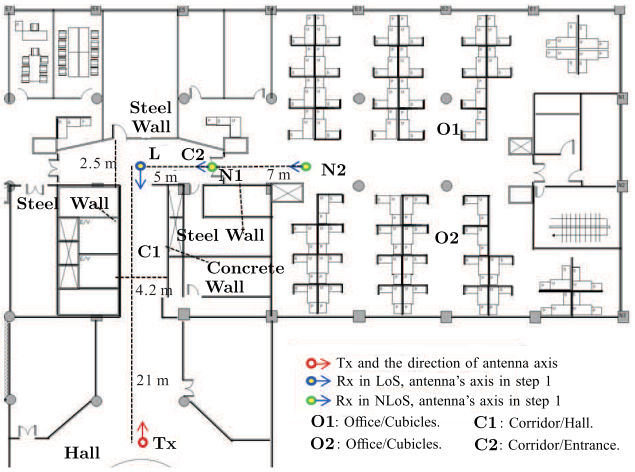

Fig. 3. The map of the indoor environment where the measurements were conducted.

Fig. 3 depicts the map of the measurement environment. To the right of the map exist two office environments "O1" and "O2" with regularly aligned cubicles separated by cardboard. To the left of the map, a wide entrance hall connects to the corridor marked with "C1", and further to the entrance "C2". During the campaign, the Tx was located in the entrance hall to the bottom of the map. Fig. 4(a) shows a picture of the Tx. The axis of Tx horn antenna was pointed towards the corridor "C1" during all measurements. Three Rx's locations were considered, which include a line-of-sight (LoS) position marked with "L", and two non-line-of-sight (NLoS) positions denoted with "N1" and "N2" respectively. The location "N1" is within the corridor "C2" and close to the conjunction of corridors. The location "N2" is in open space in the office regions "O1" and "O2", where many tables and cardboard exist with various kinds of devices loaded on the tables. Figs. 4 (b), (c) and (d) illustrate the pictures of the Rx when it was located at the positions "L", "N1" and "N2" respectively. The arrows drawn in the map close to the positions "L", "N1" and "N2" specify the 0°-azimuth orientations of the Rx antenna. The Tx and Rx

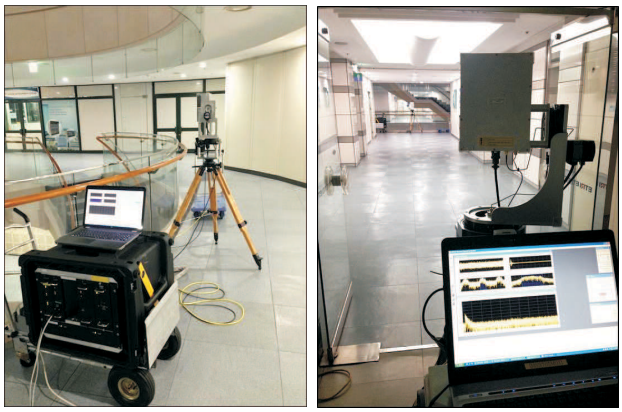

(a) Tx located at the mark "Tx"

(b) Rx located at the mark "L"

(c) Rx located at the mark "N1"

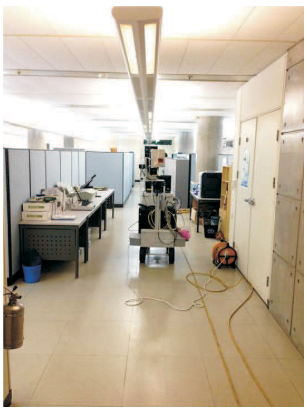

(d) Rx located at the mark "N2"

Fig. 4. The pictures of the Tx (a) and Rx in the LoS scenario (b), Rx in the NLoS-N1 (c), and in NLoS-N2 scenarios during the campaign.

antennas have the same height of 1.5 m above the ground in all measurements. The environment was stationary with no objects or humans moving. These propagation scenarios usually occur for device to device (D2D) communications in indoor environments.

The Rx antenna response at the E-plane was measured in an anechoic chamber with azimuth varying from −90° to 90°. Figs. 5(a) and 5(b) illustrate respectively the magnitude and phase of antenna radiation at the E-plane in a polar coordinate. Here, 0°-azimuth refers to the azimuth of antenna's mean-beam. For notational convenience, we use $c(\mathbf{\Omega})$ to denote the Rx antenna response at the E-plane, with the direction $\mathbf{\Omega} = [\cos(\phi), \sin(\phi)]^{\mathrm{T}}$ where ϕ is the azimuth and $(\cdot)^{\mathrm{T}}$ denotes the transpose operation. Moreover, we use $c_n(\mathbf{\Omega})$ to represent the antenna response when the antenna is rotated at the n^{th} step in azimuth, where $n = 1, 2, \ldots, N$ with N being the total number of steps. Under the assumption that the location of the antenna's feed port is fixed during scanning, and that the radiation pattern does not change when the antenna is rotated, $c_n(\mathbf{\Omega})$ can be calculated as:

$$c_n(\mathbf{\Omega}) = c\big(\boldsymbol{J}(\bar{\phi}_n)\mathbf{\Omega}\big), \tag{1}$$

IEEE Access
The journal for rapid open access publishing

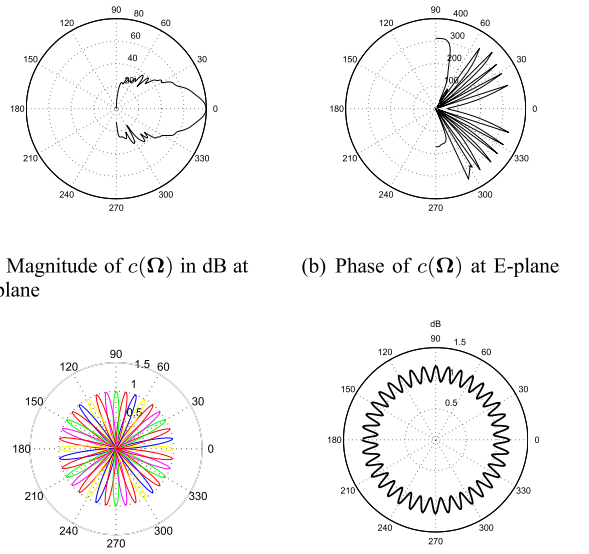

(a) Magnitude of $c(\boldsymbol{\Omega})$ in dB at E-plane

(b) Phase of $c(\boldsymbol{\Omega})$ at E-plane

(c) Magnitude of $c_n(\boldsymbol{\Omega})$, $n = 1, 2, \ldots, 36$ at E-plane

(d) Array gain $\|\boldsymbol{c}(\boldsymbol{\Omega})\|$ in dB at E-plane

Fig. 5. (a): The magnitude and (b): the phase of the 10°-HPBW Rx horn antenna response $\boldsymbol{c}(\Omega)$ in azimuth; (c): the magnitude of $c_n(\Omega)$, $n = 1, 2, \ldots, 36$, and (d): the array gain $\|\boldsymbol{c}(\Omega)\|$ represented in dB for the virtual array formed by scanning in azimuth at 36 steps in [0°, 360°).

where $\boldsymbol{J}(\bar{\phi}_n)$ is a Jones matrix:

$$\boldsymbol{J}(\bar{\phi}_n) = \begin{bmatrix} \cos(\bar{\phi}_n) & -\sin(\bar{\phi}_n) \\ \sin(\bar{\phi}_n) & \cos(\bar{\phi}_n) \end{bmatrix} \tag{2}$$

with $\bar{\phi}_n = (n-1)\Delta\phi$. Here, $\Delta\phi$ is the step size. A virtual antenna array can then be formulated with array response $\boldsymbol{c}(\boldsymbol{\Omega}) = [c_1(\boldsymbol{\Omega}), c_2(\boldsymbol{\Omega}), \ldots, c_N(\boldsymbol{\Omega})]^{\mathrm{T}}$. Fig. 5(c) demonstrates the magnitude $|c_n(\boldsymbol{\Omega})|$ versus ϕ with $n = 1, \ldots, 36$ and $\Delta\phi = 10°$. The array gain calculated as the norm $\|\boldsymbol{c}(\boldsymbol{\Omega})\|$ is depicted with respect to ϕ in Fig. 5(d).[2] It is observed that the array gain fluctuates in azimuth with a dynamic range of 0.25 dB.

III. PARAMETER ESTIMATION

According to the diagram shown in Fig. 1, the baseband representation of the received signals at the output of the Rx horn antenna being rotated by n steps when the Tx horn antenna transmits can be written as:

$$y_n(t) = \sum_{\ell=1}^{L} \alpha_\ell c_n(\boldsymbol{\Omega}_\ell) u(t-\tau_\ell) + w_n(t), \ t \in [0, T), \tag{3}$$

where $u(t)$ is the transmitted signal, T represents the sounding duration with Tx and Rx antennas fixed, τ_ℓ, $\boldsymbol{\Omega}_\ell$ and α_ℓ represent respectively the delay, direction of arrival (DoA), and complex attenuation coefficient of the ℓth propagation path, L denotes the total number of propagation paths, and $w_n(t)$ is the complex-valued circularly symmetric Gaussian random noise component. For notational convenience, we use $\boldsymbol{\Theta}$ to denote all the parameters characterizing the components in the propagation channel:

$$\boldsymbol{\Theta} = [\tau_\ell, \boldsymbol{\Omega}_\ell, \alpha_\ell; \ell = 1, \ldots, L].$$

A SAGE algorithm can be implemented which updates the estimates of $\boldsymbol{\Theta}$ iteratively [12]. For the case considered here, the admissible hidden data space $\boldsymbol{X}$ is defined as the contribution of individual propagation paths, i.e. $\boldsymbol{X} = \boldsymbol{x}_\ell(t) \in \mathcal{C}^N$ with the nth entry written as:

$$x_{\ell,n}(t) = \alpha_\ell c_n(\boldsymbol{\Omega}_\ell) u(t-\tau_\ell) + w_n(t), \ t \in [0, T). \tag{4}$$

An objective function $\Lambda(\tau, \boldsymbol{\Omega})$ that is maximized for updating the estimates $\hat{\tau}_\ell$, $\hat{\boldsymbol{\Omega}}_\ell$ is calculated as:

$$\Lambda(\tau, \boldsymbol{\Omega}) = \frac{1}{G(\boldsymbol{\Omega})} \Big| \sum_{n=1}^{N} c_n^*(\boldsymbol{\Omega}) \int_0^T x_{\ell,n}(t) u^*(t-\tau) \mathrm{d}t \Big|^2 \tag{5}$$

with $(\cdot)^*$ being the complex conjugate operation, and $G(\boldsymbol{\Omega})$ being the normalization factor:

$$G(\boldsymbol{\Omega}) = \|\boldsymbol{c}(\boldsymbol{\Omega})\|^2 \int_0^T |u(t)|^2 \mathrm{d}t. \tag{6}$$

Once $\hat{\tau}_\ell$ and $\hat{\boldsymbol{\Omega}}_\ell$ are obtained, the estimate $\hat{\alpha}_\ell$ of amplitude can be computed as

$$\hat{\alpha}_\ell = G(\hat{\boldsymbol{\Omega}}_\ell)^{-1} \sum_{n=1}^{N} c_n^*(\hat{\boldsymbol{\Omega}}_\ell) \int_0^T x_{\ell,n}(t) u^*(t-\hat{\tau}_\ell) \mathrm{d}t. \tag{7}$$

Readers can refer to [12] for the description of iterative operations in the SAGE algorithm and results of performance evaluation. The integrals shown in (5-7) are approximated by the summation of the discrete observations.

According to [12], the Cramér-Rao lower bound (CRLB) for mean square estimation error (MSEE) of unknown parameters obtained by the SAGE algorithm is inversely proportional to the array gain. From Fig. 5(c) we observed that the array gain varies with respect to azimuth, and the differences are less than 0.25 dB. This implies that the MSEE fluctuation attributed to non-constant array gain is upper-bounded by 0.25 dB [12, Appendix C]. Practically, such a variation is considered small, and the influence on parameter estimation is negligible. Therefore, the estimation results obtained by using the SAGE algorithm are considered applicable for channel characterization in this work.

In our case, since the antenna response at E-plane is available, the SAGE algorithm is applied to estimating the azimuth of arrival (AoA) ϕ_ℓ, delay τ_ℓ and complex amplitude α_ℓ for individual MPCs, under the assumption that MPCs arrive at the Rx antenna with elevations of arrival (EoA) equal to the elevation $\tilde{\theta}$ of Rx antenna axis. Strictly speaking, this assumption is unrealistic since the HPBW of the pyramid horn antenna at H-plane is equal to 10°, meaning

[2] As the antenna pattern is only measured in E-plane within the azimuth range of $[-90°, 90°]$, the response for the azimuths not being measured is assumed to be 0. Since the main lobe of the antenna is in the azimuth range $[-90°, 90°]$, the impact of such a "zero-padding" operation is considered negligible on the performance of the SAGE algorithm.

that the paths of EoAs within $[\tilde{\theta} - 5°, \tilde{\theta} + 5°]$ can still be received by the antenna. When the SAGE algorithm is executed with model mismatch in cases where the true EoAs of paths are different with $\tilde{\theta}$, estimation errors occur according to [39, Fig. 4]. In our measurements, the Rx antenna axis has three co-elevations, i.e. $\tilde{\theta} \in \{-10°, 0°, 10°\}$. Thus, for every Rx location we obtain three sets of estimated MPCs which are assumed with co-elevations equal to $-10°$, $0°$ and $10°$ respectively.

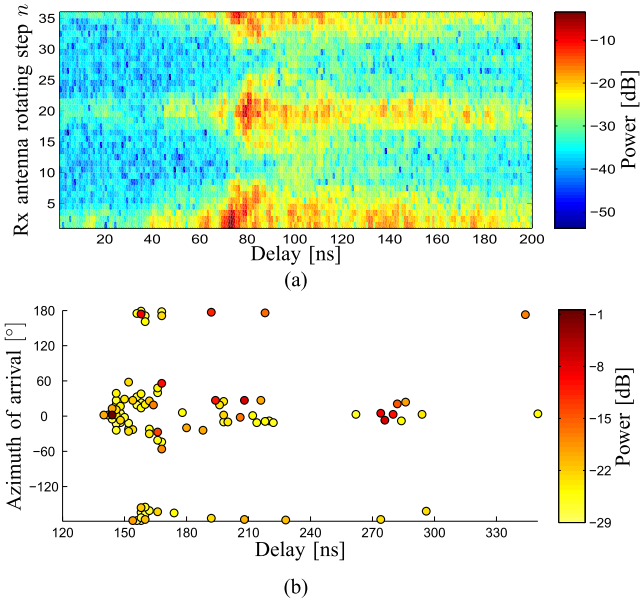

Fig. 6. Concatenated PDPs in LoS scenario, with $\tilde{\theta} = 0°$, and the MPCs estimated by using the SAGE algorithm. (a) Concatenated PDPs calculated from 36 CIRs. (b) MPCs estimated by using the SAGE algorithm.

As an example, Fig. 6(a) illustrates concatenated PDPs for 36 channels observed when the Rx antenna is rotated from 1st step to 36th step in the LoS scenario with the Rx antenna's co-elevation equal to 0°. It can be observed that the PDP obtained with the Rx antenna rotating at the first step exhibits a strong peak which corresponds to the LoS component, and the PDP obtained at the 18th step also exhibits peak attributed to the NLoS component which is generated by reflection from the steel wall located at the end of the corridor "C1". Fig. 6(b) depicts the scatter-plot of 100 MPCs estimated from the 36 CIRs. These MPCs have power at least 3 dB larger than the noise level. It is observed from Fig. 6(b) that MPCs with higher power are concentrated around AoAs 0° and 180°, corresponding to the LoS path and NLoS paths respectively.

To further evaluate the performance of the SAGE algorithm, we calculate the Bartlett delay-AoA power spectrum (PS) $p(\tau, \phi)$ for the original CIRs, the PS $\hat{p}(\tau, \phi)$ for the reconstructed CIRs computed based on the MPCs estimated and with antenna radiation pattern and system responses embedded, and the PS $\check{p}(\tau, \phi)$ for the residuals which are obtained by subtracting the reconstructed CIRs from their original counterparts [40], [41]. These PSs are illustrated in Figs. 7(a), 7(b) and 7(c) respectively. It can be observed that $p(\tau, \phi)$ and $\hat{p}(\tau, \phi)$ are similar. The maximum of $\check{p}(\tau, \phi)$ is 20-dB lower than the maximal spectral height of the original PS. These results demonstrate that by estimating 100 MPCs using the SAGE algorithm, dominant channel components with the power confined in 20 dB dynamic range can be extracted from the original CIRs.

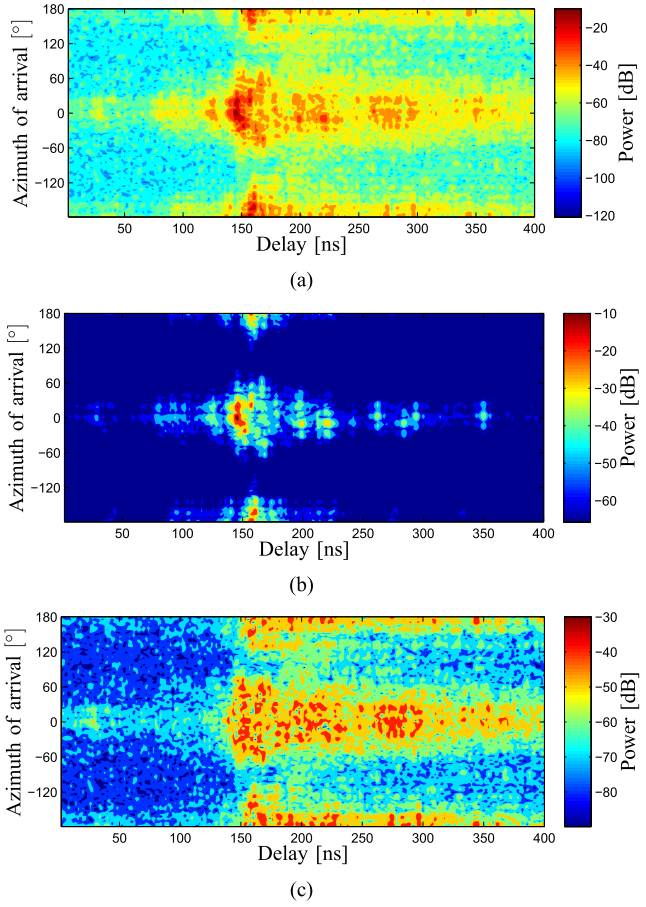

Fig. 7. The SAGE estimation results, power azimuth-delay spectra calculated based on the original received data, the reconstructed signal computed based on the SAGE estimates of multipath components, and the residual signals for a LoS scenario. (a) The AoA-delay power spectrum of original CIRs. (b) The AoA-delay power spectrum of reconstructed CIRs. (c) The AoA-delay power spectrum of residuals.

Note that during the measurements, the horn antenna may not be rotated with its feeding port fixed exactly, thus the antenna radiation pattern observed when the antenna points towards a certain direction could be different from the original pattern with axis shifted. Furthermore, the cable connected to the antenna may introduce additional non-uniform phase drifts when the antenna is rotated, and these phase variations are hard to calibrate. Both effects can lead to the degradation of estimation accuracy achievable by using the derived SAGE algorithm. The impact on channel characterization is currently under investigation by deriving CRLBs with these imperfections taken into account and comparing to both simulation and measurement results.

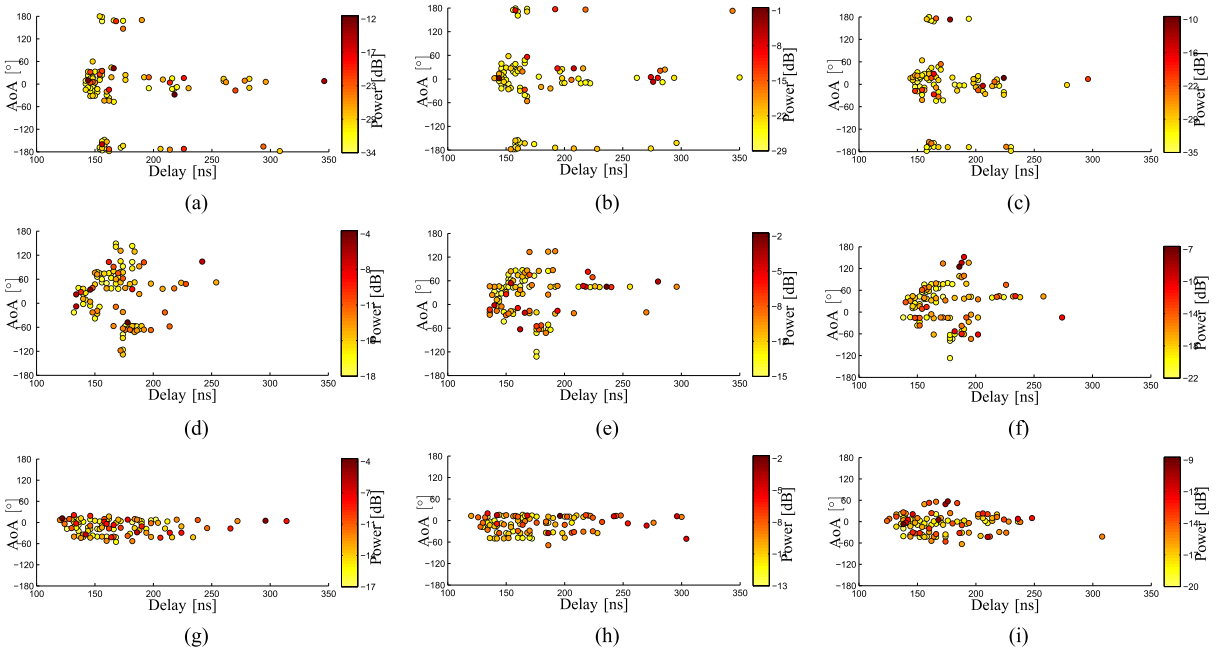

Fig. 8. Comparison of the distributions of MPCs estimated by using the SAGE estimation with Rx antenna axis directed towards different co-elevations in LoS, NLoS-N1 and NLoS-N2 scenarios. (a) LoS, $\tilde{\theta} = -10°$. (b) LoS, $\tilde{\theta} = 0°$. (c) LoS, $\tilde{\theta} = 10°$. (d) NLoS-N1, $\tilde{\theta} = -10°$. (e) NLoS-N1, $\tilde{\theta} = 0°$. (f) NLoS-N1, $\tilde{\theta} = 10°$. (g) NLoS-N2, $\tilde{\theta} = -10°$. (h) NLoS-N2, $\tilde{\theta} = 0°$. (i) NLoS-N2, $\tilde{\theta} = 10°$.

IV. CHANNEL CHARACTERISTICS IN DIFFERENT PROPAGATION SCENARIOS

Considering that channel dispersion in elevation cannot be represented effectively by using only three elevations, we focus on the characteristics in azimuth and compare the results obtained with different co-elevations of arrival in both LoS and NLoS scenarios. Figs. 8(a) to 8(i) illustrate the scatter-plots of MPCs estimated from data received with Rx antenna co-elevation $\tilde{\theta} \in \{-10°, 0°, 10°\}$ in all scenarios. It can be observed that for LoS, the MPC with the highest power observed with $\tilde{\theta} = 0°$ is stronger than the MPCs obtained with $\tilde{\theta} = -10°$ and $10°$ by more than 10 dB. This power difference reduces to only 2 dB in the NLoS scenarios, an implication that the LoS MPC contributes significantly to the channel for 28 GHz wave propagation in the indoor environments considered here. In addition, from Figs. 8(a) to 8(i) it is observed that for the LoS scenario, the MPCs' AoAs concentrate around 0° and 180°, which correspond to the LoS and NLoS paths respectively. In the NLoS scenarios, the MPCs' AoAs are widely spread within $[-120°, 120°]$ for N1 and $[-60°, 20°]$ for N2. These different constellations are correlated with the premises of the Rx. For example, in the LoS scenario, the reflected paths coming at AoA around 180° are caused by the steel wall behind the Rx, opposite to the Tx; in NLoS-N1, the Rx is located close to the conjunction between corridors "C1" and "C2", where the wall edges and complex structures around the corners scatter waves in a wide azimuthal range; in NLoS-N2, most waves arrive at the Rx from the entrance/corridor "C2", and the cubicles in regions "O1" and "O2" do not contribute too much to the overall propagation. All these observations clearly demonstrate that 28 GHz mm-wave propagation is highly dependent on the environments in the premises of Tx and Rx. This is consistent with the statement made in [36] that path constellations are simpler due to high penetration loss in mm-wave propagation. Another observation obtained from Fig. 8 is that the MPCs are widely spread in delay, but more concentrated in AoAs at one or two specific AoAs. This is more apparent in the NLoS scenarios. Such phenomena have also been observed in the measurements described in [30]. We postulate that mm-waves reverberate among a limited number of objects in the environment in such a way that the NLoS paths can have common bouncing points in their last hops before connecting to the Rx. As a result, the MPCs have similar AoAs and are well-separated in delays, leading to sparsity in the AoA domain.

Based on the MPCs estimated, we calculate the composite root-mean-square (rms) delay spreads σ_τ and AoA spreads σ_ϕ for channels, and investigate their variations with respect to the Rx antenna co-elevation. These channels are considered omnidirectional in the Rx site and directional in the Tx site with 60° azimuthal extension.

1) COMPOSITE RMS DELAY SPREAD σ_τ

Following the definition in WINNER II SCM Enhanced (SCME) [42], σ_τ is calculated as

$$\sigma_\tau = \sqrt{\overline{\tau^2} - \bar{\tau}^2}, \tag{8}$$

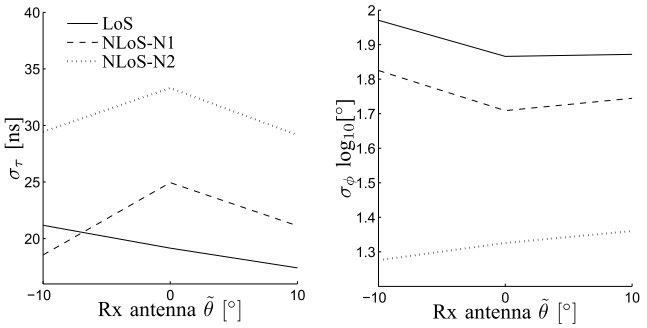

(a) Composite rms delay spread (b) Composite AoA spread

Fig. 9. Composite rms delay spread σ_τ and AoA spread σ_ϕ versus the co-elevations $\tilde{\theta}$ of Rx antenna axis for three measured locations. The legend of (a) also applies to (b).

where $\bar{\tau} = \sum_{\ell=1}^{L} \hat{\tau}_\ell \tilde{p}_\ell$ and $\overline{\tau^2} = \sum_{\ell=1}^{L} \hat{\tau}_\ell^2 \tilde{p}_\ell$ with $\tilde{p}_\ell = |\hat{\alpha}_\ell|^2 / \sum_{\ell=1}^{L} |\hat{\alpha}_\ell|^2$ denoting the normalized power of the ith MPC. Fig. 9(a) depicts σ_τ against $\tilde{\theta} \in \{-10°, 0°, 10°\}$ for LoS, NLoS-N1 and NLoS-N2 scenarios. It can be observed from Fig. 9(a) that σ_τ for NLoS-N2 is larger than other cases by approximately 10 ns. This is reasonable as in NLoS-N2, most waves arrive at the Rx from the corridor "C2", where wave reverberation among side walls generate MPCs with longer delays, as illustrated in Figs. 8(g) to 8(i). Furthermore, it is interesting to observe that in NLoS scenarios, σ_τ is larger for $\tilde{\theta} = 0°$ than $\tilde{\theta} = 10°$ and $-10°$. This implies that for NLoS propagation with Tx and Rx antennas of equal heights, channels obtained with Rx antenna titled either downwards or upwards can be less frequency selective. Such an effect is not observed in the LoS scenario.

2) COMPOSITE AoA SPREAD σ_ϕ

Fig. 9(b) depicts the variation of composite AoA spread σ_ϕ versus $\tilde{\theta}$. Here, σ_ϕ is calculated as $\sigma_\phi = \left(\sum_{\ell=1}^{L} \Delta\hat{\phi}_\ell^2 \tilde{p}_\ell\right)^{1/2}$, where $\Delta\hat{\phi}_\ell$ denotes the angle between $\hat{\mathbf{\Omega}}_\ell$ and the mean direction $\bar{\mathbf{\Omega}} = \sum_{\ell}^{L} \hat{\mathbf{\Omega}}_\ell \tilde{p}_\ell$ under the constraint of $\Delta\phi_\ell \leq 180°$ [43]. It can be observed from Fig. 9(b) that σ_ϕ is larger in LoS than in NLoS. This is reasonable since in the LoS scenario, the MPCs are concentrated in two opposite directions with AoAs 0° and 180° respectively. The average σ_ϕ represented in $\log_{10}([°])$ for LoS equals 1.9, which is higher than 1.65 as specified in the WINNER II SCME for office LoS environments [42]. For NLoS scenarios, we observed larger σ_ϕ in N1 than in N2. From the map it is seen that the objects are more uniformly distributed around the Rx in NLoS-N2 than in NLoS-N1. Thus, the observation of less σ_ϕ in NLoS-N2 is contradictory to a normal postulation that more uniformly distributed objects shall lead to a larger azimuth spread. However, from Figs. 8(g) to 8(i) it is obvious that although the Rx's premise in NLoS-N2 has more uniformly distributed objects, most MPCs have AoA within the range of $[-60°, 20°]$, i.e. they arrive at the Rx from the entrance. So the cubicles located further away from the Rx did not contribute to wave propagation, due to significant propagation loss caused by clutter environments among cubicles and long propagation distance. This phenomenon demonstrates that mm-wave propagation depends on objects in the vicinity of the communication ends, which is different from below-6 GHz propagation that can involve objects widely spread in the environment [44].

V. MULTIPATH CLUSTER CHARACTERISTICS

The effect that MPCs in a channel can be grouped as clusters has been described in many existing models for below-6 GHz wave propagation, such as Saleh-Valenzula models [45] and WINNER-alike SCMEs [42]. It is also important to investigate the clustering behavior of MPCs in 28 GHz channels. In this section, a clustering method is introduced, and then cluster characteristics and statistics extracted from measurements are elaborated.

Conventionally, clustering methods based on visual inspection, K-power-means, and Multipath Component Distance (MCD) have been applied to grouping MPCs [46]–[48]. Visual inspection is difficult to implement when the MPC's parameters are in multi-dimensions. The K-power-means approach requires an initial guess of cluster number which is hard to obtain in advance [49]. In this work, a MCD-based method similar to the CLEAN algorithm [50] is used to group MPCs, which has been proved feasible in literature such as [51].

The MCD between the ith and jth MPCs ($i \neq j$) in the case considered here is calculated as

$$\mathrm{MCD}_{ij} = \sqrt{\mathrm{MCD}_{\mathrm{AoA},ij}{}^2 + \mathrm{MCD}_{\tau,ij}{}^2}, \tag{9}$$

where $\mathrm{MCD}_{\mathrm{AoA},ij}$ is the AoA MCD calculated as

$$\mathrm{MCD}_{\mathrm{AoA},ij} = \|\mathbf{\Omega}_j - \mathbf{\Omega}_i\| \tag{10}$$

and $\mathrm{MCD}_{\tau,ij}$ represents the delay MCD:

$$\mathrm{MCD}_{\tau,ij} = \xi \frac{|\tau_i - \tau_j|}{\Delta\tau_{\max}} \frac{\sigma_\tau}{\Delta\tau_{\max}}, \tag{11}$$

where τ_i and τ_j are the delays of the ith and jth MPCs respectively, ξ is a delay scaling factor which balances the relative importance weights of AoA MCD and delay MCD, and $\Delta\tau_{\max} = \max\{|\tau_i - \tau_j|; \forall\, i, j \in [1, \ldots, L]\}$.

The clustering method adopted here consists of three steps: *Step i,* choose a reference MPC which has the largest power among all MPCs in a set eligible for extracting clusters; *Step ii,* calculate the MCD between the reference MPC and all other MPCs in the set, select the MPCs yielding MCDs less than a predefined threshold denoted with $\mathrm{MCD}_{\mathrm{th}}$, and group them together with the reference MPC as a cluster; *Step iii,* remove the MPCs already allocated to a cluster from the MPC set, and re-execute *Step i* to find the next cluster. This procedure stops until all MPCs are assigned to certain clusters. The advantage of this simple clustering method is that it is unnecessary to pre-determine the number of clusters. However, it has a drawback that the clustering result is subject to the changes of ξ and $\mathrm{MCD}_{\mathrm{th}}$. Practically, the values of ξ

and MCD_{th} are chosen by using a visual inspection method, which is viable in our case as the MPCs are distributed in two dimensions, i.e. delay and AoA domains. An empirical criterion applied for visual inspection is that the MPCs should be partitioned into clusters with clear borders. We found that $\xi = 12$ and $\text{MCD}_{\text{th}} = 0.25$ are suitable, which is consistent with the setting described in [15] and [17]. Fig. 10 illustrates two examples of clustering results obtained with the proposed method for LoS and NLoS scenarios respectively. The spots with the same color represent the MPCs assigned to a common cluster. These results are considered acceptable since most clusters identified are well-separated in delay and AoA domains.

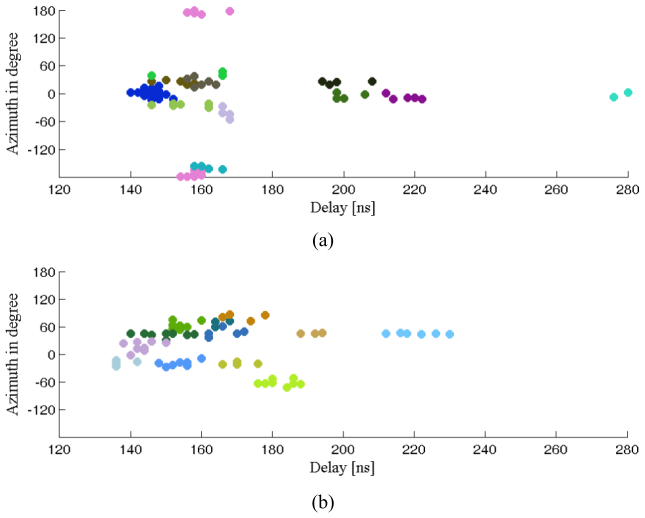

Fig. 10. **Clustering results based on the MPCs estimated from the measurements in LoS and NLoS-N1 scenarios with the Rx antenna axis coelevation $\tilde{\theta} = 0°$. (a) Multipath clusters in LoS scenario with Rx antenna axis $\tilde{\theta} = 0°$. (b) Multipath clusters in NLoS-N1 scenario with Rx antenna axis $\tilde{\theta} = 0°$.**

It is worth mentioning that the conventional multipath clusters are identified from MPCs estimated from multiple independent channel observations [42]. However, in our case, rotating antennas mechanically is so time-consuming that measuring a channel with more realizations is practically prohibitive. From the results shown in Fig. 10 it is observed that with MPCs estimated from a single channel snapshot, clusters are still extractable. This, according to our conjecture, is due to the de-embedding effect and the high resolutions in delay and AoA achieved by using the SAGE algorithm. In the sequel, cluster characteristics, including cluster number, cluster distribution in delay and AoA, cluster spread, as well as the correlation of intra-cluster dispersion in AoA and delay are investigated. Nevertheless, it is recommended to consider using efficient approaches to obtain multiple independent snapshots through DSS in order to construct accurate stochastic channel models with realistic ergodicity.

NUMBER OF CLUSTERS PER CHANNEL

Table 2 reports the number C of clusters and the number M of MPCs per cluster identified in nine propagation scenarios

TABLE 2. **Number C of clusters and number M of MPCs per cluster identified in all measurement scenarios considered in the campaign.**

Scenarios		Rx antenna axis coelevation		
		$\tilde{\theta} = -10°$	$\tilde{\theta} = 0°$	$\tilde{\theta} = 10°$
LoS	C	10	12	12
	M	7.4	5.8	5.2
NLoS-N1	C	11	12	12
	M	4.6	4.3	3.9
NLoS-N2	C	10	11	14
	M	6.3	5.8	5

with Rx antenna rotated towards different elevations $\tilde{\theta}$ in LoS and NLoS cases. It is seen from Table 2 that the total number of clusters per channel is around 12 with no significant variation versus $\tilde{\theta}$ in all three scenarios. This figure is close to that reported for below-6 GHz channels, e.g. 12 to 16 in the WINNER II SCME for office environments [42], but is quite different to the values reported in other 28 GHz channel measurements, e.g. in [31], 2 to 5 clusters were found in average in in-building LoS and NLoS scenarios. We postulate that the observation of more clusters in a channel is caused by two reasons: *i),* the Tx and Rx were surrounded by the walls of corridors and entrance, which allows most objects in the Tx and Rx premises actively involved in the propagation; and *ii)* high resolution in both delay and AoA domains achieved by using the SAGE algorithm makes it possible to extract MPCs with lower power which can be grouped as more clusters as demonstrated in Figs. 10(a) and 10(b).

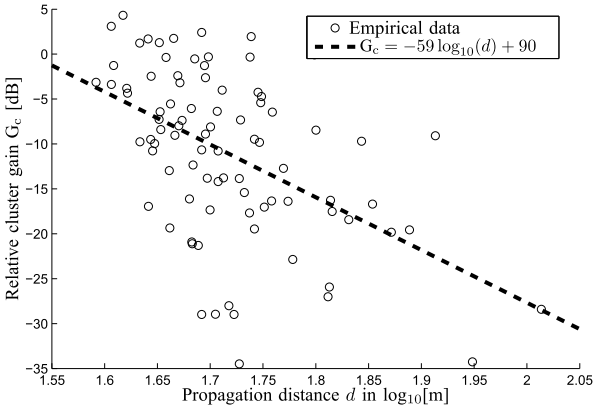

Fig. 11. **Empirical and fitted line for relative cluster gains G_c represented in dB versus propagation path length denoted in $\log_{10}$[m].**

CLUSTER GAIN AND SHADOW FADING

Fig. 11 illustrates relative cluster gain G_c in dB calculated as the total power of the MPCs allocated to a common cluster versus the average propagation length of these MPCs represented in logarithmic scale [16]. It can be observed that a linear regression line fits well with the empirical scatter plots, and the slope of the line, which corresponds to the exponent constant of a cluster path loss model, is found to be 5.9. Fig. 12 demonstrates the empirical cumulative distribution function (cdf) of the cluster shadow fading

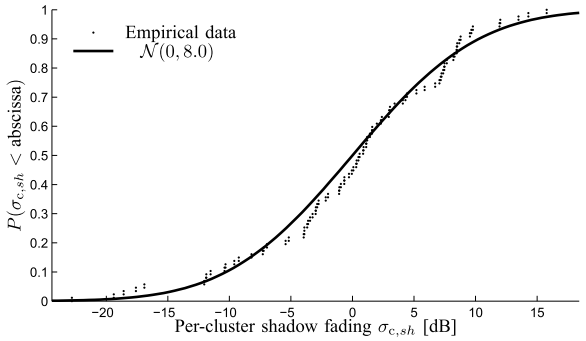

Fig. 12. **Empirical and fitted cdfs for cluster shadowing represented in dB.**

which is calculated by subtracting the cluster gain predicted from the fitted line in Fig. 11 for specific distances from the cluster power. We observed that the empirical cluster shadow fading can be fitted by log-normal distribution with mean of zero dB and standard deviation of 8 dB. The Kolmogorov-Smirnov testing is used to verify whether the null hypothesis that both empirical and the fitted cdfs are drawn from the same distributions is true. Without specifically mentioned, the fitted distributions presented in this paper have passed the Kolmogorov-Smirnov testing and proved to fit well with their empirical counterparts.

DISTRIBUTION OF CLUSTERS IN AoA AND DELAY

Fig. 13 illustrates the distributions of the clusters identified for different Rx antenna's co-elevations in three measurement scenarios. For representational convenience, the 3-dB contour of a bi-variate normal distribution's pdf, which coincides with an ellipse, is used to approximate the shape of a cluster. Specifically, the pdf has its first moment equal to the center of gravity (CoG) of a cluster, standard deviations identical with the cluster's spreads in delay and AoA, and the bi-variate correlation coefficient being the same as the correlation coefficient of the MPCs' AoA and delay deviations from the cluster CoG. The ellipses' colors represent the relative dB scale of cluster power. For comparison convenience, the largest cluster power found in each scenario is normalized to 0 dB. Furthermore, we adopt the same ranges for $x-$ and $y-$ axis, as well as identical color-to-power scaling in all nine plots shown in Fig. 13. The following observations are obtained: *i)* clusters detected in the LoS scenario have a larger dynamic range of power variation than in the NLoS scenarios; *ii)* clusters are widely spread in delay in all nine plots;

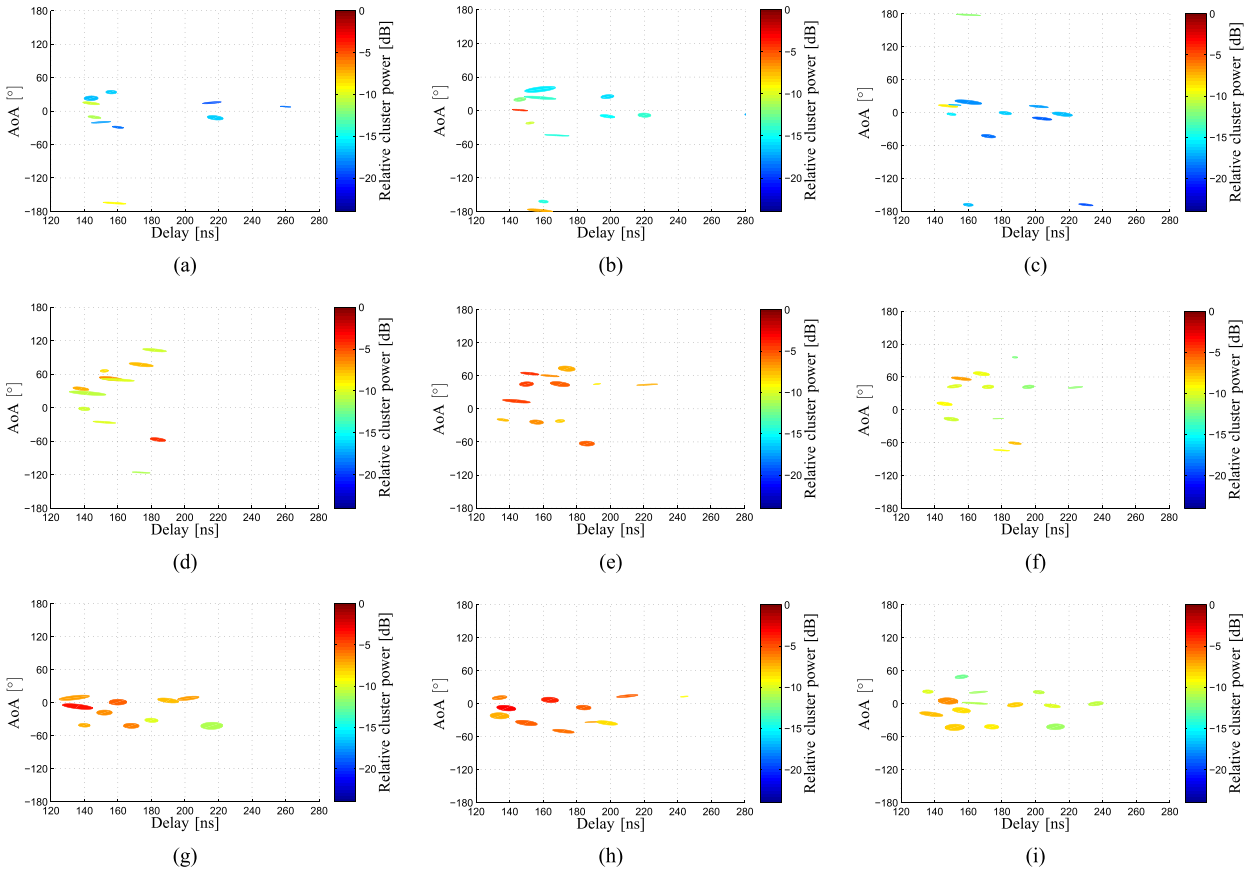

Fig. 13. **Multipath clusters represented as ellipses, each calculated as the 3-dB contour of a bi-variate normal pdf parameterized with individual clusters' center of gravity, the spreads in AoA and delay, as well as the correlation coefficient between the spreads. (a) LoS scenario, Rx $\tilde{\theta} = -10°$. (b) LoS scenario, Rx $\tilde{\theta} = 0°$. (c) LoS scenario, Rx $\tilde{\theta} = 10°$. (d) NLoS-N1 scenario, Rx $\tilde{\theta} = -10°$. (e) NLoS-N1 scenario, Rx $\tilde{\theta} = 0°$. (f) NLoS-N1 scenario, Rx $\tilde{\theta} = 10°$. (g) LoS-N2 scenario, Rx $\tilde{\theta} = -10°$. (h) NLoS-N2 scenario, Rx $\tilde{\theta} = 0°$. (i) NLoS-N2 scenario, Rx $\tilde{\theta} = 10°$.**

iii) except for NLoS-N1, the clusters are concentrated in narrow regions in AoA, which is reasonable since the location "N1" is close to the corner of the corridor "C2", where the environment is more cluttered than in other cases; *iv)* clusters exhibit similar intra-cluster spreads in AoA for LoS and NLoS scenarios, and the clusters in LoS exhibit smaller spreads in delay than in NLoS scenarios; *v)* for different Rx antenna elevations, we observed significant changes in cluster constellations, which implies that a channel changes significantly when being observed at different elevations.

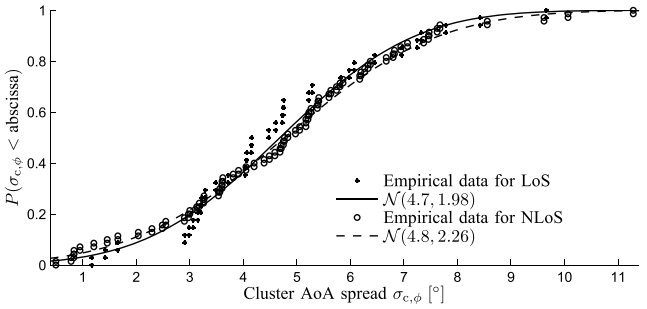

Fig. 14. Empirical cdfs and fitted cdfs $P(\sigma_{c,\phi} <$ abscissa$)$ of cluster AoA spread $\sigma_{c,\phi}$ for LoS and NLoS scenarios.

CLUSTER AoA SPREAD $\sigma_{c,\phi}$

Fig. 14 depicts the empirical cdfs $P(\sigma_{c,\phi} <$ abscissa$)$ for the cluster AoA spread $\sigma_{c,\phi}$ in both LoS and NLoS scenarios. The cdf for NLoS was calculated with all clusters observed from the channels with multiple Rx antenna elevations in two NLoS scenarios. In Fig. 14, the fitted normal distributions with properly selected parameters are illustrated. It is observed from Fig. 14 that $\sigma_{c,\phi}$ in LoS and NLoS scenarios follows similar distributions. Comparing with the statistics of cluster AoA spread reported in WINNER II SCME [42], we found that the mean $\sigma_{c,\phi}$ in 28 GHz channels measured here is about 4.8°, close to 5° as reported in A1 office environments for below-6 GHz channels [42]. This observation is contradictory to a conventional opinion that mm-wave propagation channels usually exhibit larger cluster angular spreads than the channels in lower frequencies, due to significant scattering effects in mm-wave bands. We postulate that large cluster azimuth spread is not observed in our cases for mm-wave channels, because the high-resolution in delay and AoA provided by the SAGE algorithm allows partitioning MPCs into clusters with smaller delay and AoA extensions.

CLUSTER DELAY SPREAD $\sigma_{c,\tau}$

Fig. 15 depicts the empirical and fitted cdfs $P(\sigma_{c,\tau} <$ abscissa$)$ of cluster delay spread $\sigma_{c,\tau}$ for LoS and NLoS scenarios. The cdfs of lognormal distributions fit well to the empirical data. It is observed from Fig. 15 that the average $\sigma_{c,\tau}$ is $10^{-8.6} \approx 2.5$ ns and $10^{-8.4} \approx 4.2$ ns for LoS and NLoS scenarios respectively, i.e. clusters have larger extensions in delay in NLoS than in LoS scenarios. This is reasonable as more objects can be involved in propagation

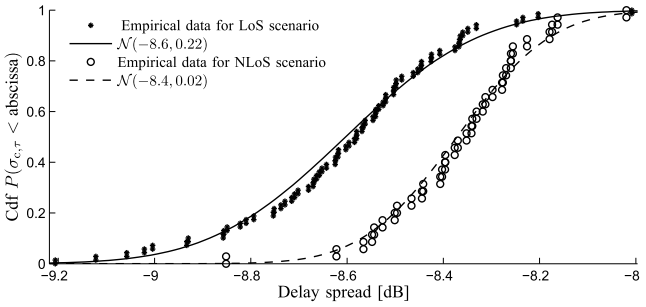

Fig. 15. Empirical cdfs and fitted cdfs $P(\sigma_{c,\tau} <$ abscissa$)$ of cluster delay spread $\sigma_{c,\tau}$ for LoS and NLoS scenarios.

for NLoS scenarios, and they contribute with a large amount of paths which are eventually grouped to clusters with larger spreads in delay domain.

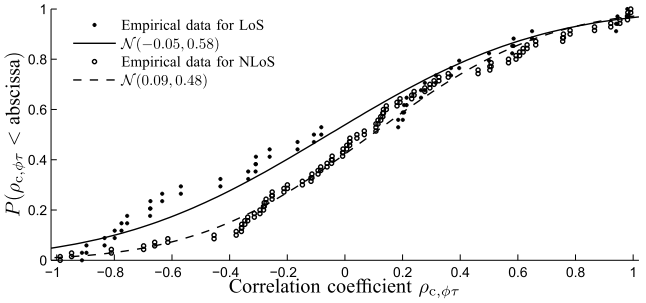

Fig. 16. Empirical cdfs and fitted cdfs $P(\rho_{c,\phi\tau} <$ abscissa$)$ of correlation coefficient $\rho_{c,\phi\tau}$ between delay and AoA dispersion in a cluster for LoS and NLoS scenarios.

CORRELATION COEFFICIENT $\rho_{c,\phi\tau}$ BETWEEN INTRA-CLUSTER PATH DISTRIBUTION IN DELAY AND AoA

Fig. 16 depicts the empirical cdfs $P(\rho_{c,\phi\tau} <$ abscissa$)$ of correlation coefficient $\rho_{c,\phi\tau}$ between the delay and AoA distributions of MPCs assigned in a cluster for LoS and NLoS scenarios. The cdfs of normal distributions with appropriately selected parameters can fit well with the empirical graphs as illustrated in Fig. 16. It is observed that $\rho_{c,\phi\tau}$ is widely distributed within $[-1, 1]$ for both LoS and NLoS scenarios. Since the shape of a two-dimensional cluster, represented by the intra-cluster path distribution in AoA and delay, is jointly determined by $\rho_{c,\phi\tau}$, $\sigma_{c,\tau}$, and $\sigma_{c,\phi}$, we may deduce from the wide dispersion of $\rho_{c,\phi\tau}$ that, the shape of the clusters is quite diverse in both LoS and NLoS scenarios, which is consistent with the observation of differently titled ellipses as shown in Fig. 13.

Table 3 compares the statistical parameters for composite and cluster-level channel characteristics obtained from our measurements and from literature for 28 GHz mm-wave propagation. The counterparts in WINNER II SCMEs and relevant literature for below 6 GHz channels are also shown. It is observed from Table 3 that for 28 GHz channels, more clusters are found in the measurements considered here than in those reported in [31] and [52]. Furthermore, we observe

similar number of MPCs per cluster for LoS and NLoS cases, which is different from the phenomenon reported in [31] that the number of MPCs per cluster is significantly larger in NLoS than in LoS scenarios. We postulate that this difference is caused by the SAGE algorithm capable of de-embedding system and antenna responses from original channel observations. Benefiting from higher resolutions in resolving MPCs, the clusters are separated with clearer borders than those observed by using non-parametric approaches [31].

TABLE 3. Comparison of channel model parameters extracted in this work, reported in literature [31], [52] for 28 GHz wave propagation, and in the WINNER II SCMEs [46, Tables 4 and 5] and literature [53] for below-6 GHz channels.

Parameters\ Scenarios		28 GHz, here		28 GHz†		WINNER A1	
		LoS	NLoS	LoS	NLoS	LoS	NLoS
σ_τ $[\log_{10}([s])]$	μ	-7.7	-7.6	-7.9	-7.7	-7.42	-7.60
	σ	0.06	0.13	-	-	0.27	0.19
σ_ϕ $[\log_{10}([°])]$	μ	1.9	1.54	2.84°	21.88°	1.65	1.69
	σ	0.05	0.24	5.32°	17.49°	0.26	0.14
C	μ	11	12	1.82	3.14	12	16
	σ	1.15	1.37	1.5	2.2	-	-
M	μ	6.04	4.9	5.17	10.91	20	20
	σ	5.5	3.9	0.63	1.01	-	-
$\sigma_{c,\tau}$ $[\log_{10}(s)]$	μ	-8.6	-8.4	-	-	-8.22*	-8.03*
	σ	0.22	0.02	-	-	-	-
$\sigma_{c,\phi}[°]$	μ	4.7	4.8	4.72	11.84	2.6*	11.2*
	σ	1.98	2.26	2.69	13.35	1.3*	1.4*
$\rho_{c,\phi\tau}$	μ	-0.05	0.09	-	-	-	-
	σ	0.58	0.48	-	-	-	-

C: Number of clusters in a channel
†: According to the results reported in [32], [57]
*: According to the updates of the SCMEs in [58]

For the comparison between 28 GHz and below-6 GHz channels, it is seen from Table 3 that in LoS scenarios, 28 GHz channels exhibit less composite rms delay spread and larger composite AoA spread, and for NLoS scenarios, the composite channel behaviors are similar. In general, clusters with smaller size especially in angular domains are more likely to be observed in 28 GHz channel than in below-6 GHz channels. Furthermore, it is obvious from Table 3 that by using the SAGE in extracting MPCs, the model parameters obtained here for 28 GHz propagation do not have significant differences to those for below-6 GHz channels, although the 28 GHz channel does exhibit significant sparsity in angular domains compared with the channels below-6 GHz as reported in [54].

VI. CONCLUSIONS

In this paper, cluster-based characterization was applied to analyzing indoor propagation channels measured in 28 GHz millimeter (mm)-wave frequency bands in office environments. A Space-Alternating Generalized Expectation-maximization (SAGE) algorithm was implemented to extract multipath components (MPCs) from the output of a virtual antenna array generated by rotating a horn antenna in steps. Based on estimated MPCs, clusters were identified using a simplified multipath-component-distance approach. Stochastic behaviors of composite channel delay spread, azimuth of arrival (AoA) spread, and cluster characteristics, such as cluster number, delay spread, AoA spreads, and spread correlation have been investigated for line-of-sight (LoS) and non-line-of-sight (NLoS) scenarios. These results showed that in general, the mm-wave channels exhibit simpler multipath constellation. Their small-scale characteristics are dependent on the environments surrounding the transmitter and receiver, and consequently, channels exhibit significant sparsity in the angular domain. In addition, the high-resolution achieved jointly by using wideband sounding signals and the SAGE algorithm allows detecting more clusters with clear separations in delay and AoA. The cluster characteristics for 28 GHz channels are similar with those specified in conventional spatial models for below-6 GHz channels. These studies demonstrate the potentiality of applying high-resolution parameter estimation e.g. by using the specular-path-based SAGE algorithm to extract channel characteristics and the easiness of extracting cluster statistics of multipath from estimation results.

REFERENCES

[1] J. G. Andrews *et al.*, "What will 5G be?" *IEEE J. Sel. Areas Commun.*, vol. 32, no. 6, pp. 1065–1082, Jun. 2014.
[2] T. Jämsä, P. Kyösti, and K. Kusume, *Deliverable d1.2 Initial Channel Models Based on Measurements*, Project Name: Mobile and Wireless Communications Enablers for the Twenty-Twenty Information Society (METIS), document ICT-317669-METIS/D1.2, 2014.
[3] R. C. Daniels and R. W. Heath, "60 GHz wireless communications: Emerging requirements and design recommendations," *IEEE Veh. Technol. Mag.*, vol. 2, no. 3, pp. 41–50, Sep. 2007.
[4] P. F. M. Smulders, "Statistical characterization of 60-GHz indoor radio channels," *IEEE Trans. Antennas Propag.*, vol. 57, no. 10, pp. 2820–2829, Oct. 2009.
[5] N. Moraitis and A. D. Panagopoulos, "Millimeter wave channel measurements and modeling for indoor femtocell applications," in *Proc. Eur. Conf. Antenna Propag. (EuCAP)*, Lisbon, Portugal, Apr. 2015, pp. 1–5.
[6] R. J. Weiler, M. Peter, T. Kühne, M. Wisotzki, and W. Keusgen, "Simultaneous millimeter-wave multi-band channel sounding in an urban access scenario," in *Proc. Eur. Conf. Antenna Propag. (EuCAP)*, Lisbon, Portugal, Apr. 2015, pp. 1–5.
[7] L. M. Correia and P. O. Frances, "Estimation of materials characteristics from power measurements at 60 GHz," in *Proc. 5th IEEE Int. Symp. Pers., Indoor Mobile Radio Commun., Wireless Netw. (PIMRC)*, vol. 2. Hague, The Netherlands, Sep. 1994, pp. 510–513.
[8] H. Yang, P. F. M. Smulders, and M. H. A. J. Herben, "Frequency selectivity of 60-GHz LOS and NLOS indoor radio channels," in *Proc. 63th IEEE Veh. Technol. Conf. (VTC)*, vol. 6. Melbourne, VIC, Australia, May 2006, pp. 2727–2731.
[9] S. Collonge, G. Zaharia, and G. E. Zein, "Influence of the human activity on wide-band characteristics of the 60 GHz indoor radio channel," *IEEE Trans. Wireless Commun.*, vol. 3, no. 6, pp. 2396–2406, Nov. 2004.
[10] S. Piersanti, L. A. Annoni, and D. Cassioli, "Millimeter waves channel measurements and path loss models," in *Proc. IEEE Int. Conf. Commun. (ICC)*, Ottawa, ON, Canada, Jun. 2012, pp. 4552–4556.
[11] B. H. Fleury, M. Tschudin, R. Heddergott, D. Dahlhaus, and K. Ingeman Pedersen, "Channel parameter estimation in mobile radio environments using the SAGE algorithm," *IEEE J. Sel. Areas Commun.*, vol. 17, no. 3, pp. 434–450, Mar. 1999.
[12] A. Richter and R. S. Thoma, "Joint maximum likelihood estimation of specular paths and distributed diffuse scattering," in *Proc. IEEE 61st Veh. Technol. Conf. (VTC-Spring)*, vol. 1. Stockholm, Sweden, May 2005, pp. 11–15.
[13] C. Gustafson, F. Tufvesson, S. Wyne, K. Haneda, and A. F. Molisch, "Directional analysis of measured 60 GHz indoor radio channels using SAGE," in *Proc. IEEE Veh. Technol. Conf. (VTC Spring)*, Yokohama, Japan, May 2011, pp. 1–5.

[14] M.-T. Martinez-Ingles, J.-M. Molina-Garcia-Pardo, J.-V. Rodriguez, J. Pascual-Garcia, and L. Juan-Llacer, "Experimental comparison of UWB against mm-wave indoor radio channel characterization," in *Proc. IEEE Antennas Propag. Soc. Int. Symp. (APSURSI)*, Orlando, FL, USA, Jul. 2013, pp. 1946–1947.

[15] C. Gustafson, K. Haneda, S. Wyne, and F. Tufvesson, "On mm-wave multipath clustering and channel modeling," *IEEE Trans. Antennas Propag.*, vol. 62, no. 3, pp. 1445–1455, Mar. 2014.

[16] C. Gustafson, D. Bolin, and F. Tufvesson, "Modeling the cluster decay in mm-wave channels," in *Proc. 8th Eur. Conf. Antennas Propag. (EuCAP)*, Hague, The Netherlands, Apr. 2014, pp. 804–808.

[17] M. Kim, J.-I. Takada, Y. Chang, J. Shen, and Y. Oda, "Large scale characteristics of urban cellular wideband channels at 11 GHz," in *Proc. Eur. Conf. Antenna Propag. (EuCAP)*, Lisbon, Portugal, Apr. 2015, pp. 1–4.

[18] K. Belbase, M. Kim, and J.-I. Takada, "Study of propagation mechanisms and identification of scattering objects in indoor multipath channels at 11 GHz," in *Proc. Eur. Conf. Antenna Propag. (EuCAP)*, Lisbon, Portugal, Apr. 2015, pp. 1–4.

[19] T. S. Rappaport *et al.*, "Millimeter wave mobile communications for 5G cellular: It will work!" *IEEE Access*, vol. 1, pp. 335–349, May 2013.

[20] Y. Azar *et al.*, "28 GHz propagation measurements for outdoor cellular communications using steerable beam antennas in New York City," in *Proc. IEEE Int. Conf. Commun. (ICC)*, Budapest, Hungary, Jun. 2013, pp. 5143–5147.

[21] X. Wu, Y. Zhang, C.-X. Wang, G. Goussetis, E.-H. M. Aggoune, and M. M. Alwakeel, "28 GHz indoor channel measurements and modelling in laboratory environment using directional antennas," in *Proc. Eur. Conf. Antenna Propag. (EuCAP)*, Lisbon, Portugal, Apr. 2015, pp. 1–5.

[22] H. Zhao *et al.*, "28 GHz millimeter wave cellular communication measurements for reflection and penetration loss in and around buildings in New York City," in *Proc. IEEE Int. Conf. Commun. (ICC)*, Jun. 2013, pp. 5163–5167.

[23] M. Lei, J. Zhang, T. Lei, and D. Du, "28-GHz indoor channel measurements and analysis of propagation characteristics," in *Proc. IEEE 25th Annu. Int. Symp. Pers., Indoor, Mobile Radio Commun. (PIMRC)*, Sep. 2014, pp. 208–212.

[24] G. R. Maccartney, T. S. Rappaport, S. Sun, and S. Deng, "Indoor office wideband millimeter-wave propagation measurements and channel models at 28 and 73 GHz for ultra-dense 5G wireless networks," *IEEE Access*, vol. 3, pp. 2388–2424, 2015.

[25] T. S. Rappaport, G. R. Maccartney, M. K. Samimi, and S. Sun, "Wideband millimeter-wave propagation measurements and channel models for future wireless communication system design," *IEEE Trans. Commun.*, vol. 63, no. 9, pp. 3029–3056, Sep. 2015.

[26] A. Karttunen, K. Haneda, J. Järveläinen, and J. Putkonen, "Polarisation characteristics of propagation paths in indoor 70 GHz channels," in *Proc. Eur. Conf. Antenna Propag. (EuCAP)*, Lisbon, Portugal, Apr. 2015, pp. 1–4.

[27] G. R. MacCartney, J. Zhang, S. Nie, and T. S. Rappaport, "Path loss models for 5G millimeter wave propagation channels in urban microcells," in *Proc. IEEE Global Commun. Conf. (GLOBECOM)*, Atlanta, GA, USA, Dec. 2013, pp. 3948–3953.

[28] V. Semkin, U. Virk, A. Karttunen, K. Haneda, and A. V. Räisänen, "E-band propagation channel measurements in an urban street canyon," in *Proc. Eur. Conf. Antenna Propag. (EuCAP)*, Lisbon, Portugal, Apr. 2015, pp. 1–4.

[29] N. Zhang, X. Yin, S. X. Lu, M. Du, and X. Cai, "Measurement-based angular characterization for 72 GHz propagation channels in indoor environments," in *Proc. Globecom Workshops (GC Wkshps)*, Austin, TX, USA, Dec. 2014, pp. 370–376.

[30] M. Samimi *et al.*, "28 GHz angle of arrival and angle of departure analysis for outdoor cellular communications using steerable beam antennas in New York City," in *Proc. IEEE 77th Veh. Technol. Conf. (VTC Spring)*, Dresden, Germany, Jun. 2013, pp. 1–6.

[31] S. Hur, Y.-J. Cho, J. Lee, N.-G. Kang, J. Park, and H. Benn, "Synchronous channel sounder using horn antenna and indoor measurements on 28 GHz," in *Proc. IEEE Int. Black Sea Conf. Commun. Netw. (BlackSeaCom)*, Odessa, Ukraine, May 2014, pp. 83–87.

[32] S. Nie, G. R. MacCartney, Jr., S. Sun, and T. S. Rappaport, "72 GHz millimeter wave indoor measurements for wireless and backhaul communications," in *Proc. IEEE 24th Int. Symp. Pers. Indoor Mobile Radio Commun. (PIMRC)*, Sep. 2013, pp. 2429–2433.

[33] G. R. MacCartney and T. S. Rappaport, "73 GHz millimeter wave propagation measurements for outdoor urban mobile and backhaul communications in New York City," in *Proc. IEEE Int. Conf. Commun. (ICC)*, Sydney, NSW, Australia, Jun. 2014, pp. 4862–4867.

[34] G. R. Maccartney, M. K. Samimi, and T. S. Rappaport, "Omnidirectional path loss models in New York City at 28 GHz and 73 GHz," in *Proc. IEEE 25th Int. Symp. Pers., Indoor, Mobile Radio Commun. (PIMRC)*, Austin, TX, USA, Sep. 2014, pp. 227–231.

[35] X. Yin, C. Ling, M.-D. Kim, and H. K. Chung, "Parameter estimation using the sliding-correlator's output for wideband propagation channels," *EURASIP J. Wireless Commun. Netw.*, vol. 2015, no. 1, p. 165, 2015. [Online]. Available: http://jwcn.eurasipjournals.com/content/2015/1/165

[36] S. Salous, S. M. Feeney, X. Raimundo, and A. A. Cheema, "Wideband MIMO channel sounder for radio measurements in the 60 GHz band," in *IEEE Trans. Wireless Commun.*, vol. PP, no. 99, p. 1, 2015.

[37] R. J. Pirkl and G. D. Durgin, "Optimal sliding correlator channel sounder design," *IEEE Trans. Wireless Commun.*, vol. 7, no. 9, pp. 3488–3497, Sep. 2008.

[38] G. Martin, "Wideband channel sounding dynamic range using a sliding correlator," in *Proc. IEEE 51st Veh. Technol. Conf. (VTC)*, vol. 3. Tokyo, Japan, May 2000, pp. 2517–2521.

[39] M. Landmann, M. Kaske, and R. S. Thoma, "Impact of incomplete and inaccurate data models on high resolution parameter estimation in multidimensional channel sounding," *IEEE Trans. Antennas Propag.*, vol. 60, no. 2, pp. 557–573, Feb. 2012.

[40] M. S. Babtlett, "Smoothing periodograms from time-series with continuous spectra," *Nature*, vol. 161, pp. 686–687, May 1948.

[41] P. Stoica and R. L. Moses, *Introduction to Spectral Analysis*. Upper Saddle River, NJ, USA: Prentice-Hall, 1997.

[42] *WINNER II Interim Channel Models*, IST-4-027756 WINNER D1.1.1 Std, 2006.

[43] B. H. Fleury, "First- and second-order characterization of direction dispersion and space selectivity in the radio channel," *IEEE Trans. Inf. Theory*, vol. 46, no. 6, pp. 2027–2044, Sep. 2000.

[44] B. H. Fleury, X. Yin, K. G. Rohbrandt, P. Jourdan, and A. Stucki, "Performance of a high-resolution scheme for joint estimation of delay and bidirection dispersion in the radio channel," in *Proc. IEEE Veh. Technol. Conf. (VTC-Spring)*, vol. 1. May 2002, pp. 522–526.

[45] A. A. M. Saleh and R. A. Valenzuela, "A statistical model for indoor multipath propagation," *IEEE J. Sel. Areas Commun.*, vol. 5, no. 2, pp. 128–137, Feb. 1987.

[46] K. Yu, Q. Li, D. Cheung, and C. Prettie, "On the tap and cluster angular spreads of indoor WLAN channels," in *Proc. IEEE 59th Veh. Technol. Conf. (VTC Spring)*, vol. 1. May 2004, pp. 218–222.

[47] N. Czink, C. Mecklenbrauker, and G. Del Galdo, "A novel automatic cluster tracking algorithm," in *Proc. IEEE 17th Int. Symp. Pers., Indoor Mobile Radio Commun.*, Helsinki, Finland, Sep. 2006, pp. 1–5.

[48] N. Czink, G. Del Galdo, X. Yin, and C. Mecklenbrauker, "A novel environment characterisation metric for clustered MIMO channels used to validate a SAGE parameter estimator," in *Proc. 15th IST Mobile Wireless Commun. Summit*, Mykonos, Greece, Jun. 2006, pp. 1–6.

[49] N. Czink, P. Cera, J. Salo, E. Bonek, J. Nuutinen, and J. Ylitalo, "Automatic clustering of MIMO channel parameters using the multi-path component distance measure," in *Proc. Wireless Pers. Multimedia Commun. (WPMC)*, Aalborg, Denmark, Sep. 2005.

[50] J. Högbom, "Aperture synthesis with a non-regular distribution of interferometer baselines," *Astron. Astrophys. Suppl.*, vol. 15, no. no. 3, pp. 417–426, 1974.

[51] M. Steinbauer, H. Ozcelik, H. Hofstetter, C. F. Mecklenbrauker, and E. Bonek, "How to quantify multipath separation," *IEICE Trans. Electron.*, vol. E85-C, no. 3, pp. 552–557, Mar. 2002.

[52] M. R. Akdeniz *et al.*, "Millimeter wave channel modeling and cellular capacity evaluation," *IEEE J. Sel. Areas Commun.*, vol. 32, no. 6, pp. 1164–1179, Jun. 2014.

[53] C. Huang, J. Zhang, X. Nie, and Y. Zhang, "Cluster characteristics of wideband MIMO channel in indoor hotspot scenario at 2.35 GHz," in *Proc. IEEE 70th Veh. Technol. Conf. Fall (VTC-Fall)*, Sep. 2009, pp. 1–5.

[54] N. Czink, "The random-cluster model—A stochastic MIMO channel model for broadband wireless communication systems of the 3rd generation and beyond," Ph.D. dissertation, Dept. Electron. Inf. Technol., Vienna Univ. Technol., Vienna, Austria, 2007.

XUEFENG YIN received the bachelor's degree in optoelectronics engineering from the Huazhong University of Science and Technology, Wuhan, China, in 1995, and the M.S. degree in digital communications and the Ph.D. degree in wireless communications from Aalborg University, Denmark, in 2002 and 2006, respectively. From 2006 to 2008, he was an Assistant Professor with Aalborg University. In 2008, he joined Tongji University as an Associate Professor with the College of Electronics and Information Engineering, Shanghai, China. His research interests include high-resolution parameter estimation for propagation channels, channel characterization and stochastic modeling for 5G wireless communications, radar signal processing, and target recognition.

CEN LING received the bachelor's degree in electronic science and technology from the Nanjing University of Posts and Telecommunication, in 2012. She is currently pursuing the Ph.D. degree in control science and engineering with Tongji University. In 2014, she was a Visiting Ph.D. Student with the Polytechnic University of Catalonia, Spain. Her current research interests are in the fields of channel parameter estimation and modeling, cooperative communication, and network optimization.

MYUNG-DON KIM joined the Electronics and Telecommunications Research Institute (ETRI), Daejeon, Korea, in 1995, and worked on the development of mobile test-beds for CDMA, IMT-2000, and WCDMA systems. Since 2006, he has been involved in the development of wide-band channel measuring system for below 6 GHz and millimeter-wave bands, channel measurement campaign, and statistical channel modeling. He is currently a Principal Researcher with the Communications and Internet Research Laboratory, ETRI. His current research interests include millimeter-wave channel measurement and modeling for 5G mobile communications.